PAPER

Effect of rotation zero-crossing on single-fluid plasma response to three-dimensional magnetic perturbations

IOP Publishing Plasma Physics and Controlled Fusion
Plasma Phys. Control. Fusion **59** (2017) 044001 (10pp) https://doi.org/10.1088/1361-6587/aa5860

Effect of rotation zero-crossing on single-fluid plasma response to three-dimensional magnetic perturbations

B C Lyons[1,2,5], N M Ferraro[3], C Paz-Soldan[2], R Nazikian[3] and A Wingen[4]

[1] Oak Ridge Institute for Science and Education, Oak Ridge, Tennessee 37831-0117, United States of America
[2] General Atomics, San Diego, California 92121, United States of America
[3] Princeton Plasma Physics Laboratory, Princeton, New Jersey 08543-0451, United States of America
[4] Oak Ridge National Laboratory, Oak Ridge, TN 37831, United States of America

E-mail: lyonsbc@fusion.gat.com

Received 18 October 2016, revised 7 December 2016
Accepted for publication 10 January 2017
Published 14 February 2017

Abstract

In order to understand the effect of rotation on the response of a plasma to three-dimensional magnetic perturbations, we perform a systematic scan of the zero-crossing of the rotation profile in a DIII-D ITER-similar shape equilibrium using linear, time-independent modeling with the M3D-C1 extended magnetohydrodynamics code. We confirm that the local resonant magnetic field generally increases as the rotation decreases at a rational surface. Multiple peaks in the resonant field are observed near rational surfaces, however, and the maximum resonant field does not always correspond to zero rotation at the surface. Furthermore, we show that non-resonant current can be driven at zero-crossings not aligned with rational surfaces if there is sufficient shear in the rotation profile there, leading to amplification of near-resonant Fourier harmonics of the perturbed magnetic field and a decrease in the far-off-resonant harmonics. The quasilinear electromagnetic torque induced by this non-resonant plasma response provides drive to flatten the rotation, possibly allowing for increased transport in the pedestal by the destabilization of turbulent modes. In addition, this torque acts to drive the rotation zero-crossing to dynamically stable points near rational surfaces, which would allow for increased resonant penetration. By one or both of these mechanisms, this torque may play an important role in bifurcations into suppression of edge-localized modes. Finally, we discuss how these changes to the plasma response could be detected by tokamak diagnostics. In particular, we show that the changes to the resonant field discussed here have a significant impact on the external perturbed magnetic field, which should be observable by magnetic sensors on the high-field side of tokamaks but not on the low-field side. In addition, TRIP3D-MAFOT simulations show that none of the changes to the plasma response described here substantially affects the divertor footprint structure.

Keywords: magnetic perturbations, extended magnetohydrodynamics, plasma response, rotation, torque, edge-localized modes, ELM suppression

(Some figures may appear in colour only in the online journal)

1. Introduction

Externally applied three-dimensional magnetic perturbations are routinely used in modern tokamaks for a variety of purposes, including correcting error fields, controlling particle transport and mitigating or suppressing edge-localized modes (ELMs). In particular, the need to control ELMs in order to prevent intolerable heat fluxes to plasma-facing components in future tokamaks (including ITER) has driven the experimental and theoretical study of the effects of three-

[5] Author to whom any correspondence should be addressed.

dimensional magnetic perturbations on plasma equilibrium, stability and confinement. Varying degrees of mitigation or suppression have been achieved on DIII-D [1], JET [2], ASDEX Upgrade [3], KSTAR [4], MAST [5] and EAST [6].

Despite the successes of experimental campaigns, a predictive theoretical understanding for how magnetic perturbations suppress ELMs is still incomplete. Early theoretical explanations focused on the nature of the applied vacuum field. In particular, it was noted that the vacuum resonant magnetic perturbations (RMPs) could couple to the equilibrium magnetic field to open magnetic islands. If the RMPs were strong enough, the opened islands could overlap, producing a region of stochasticity in the edge-pedestal region. The increased radial transport in this stochastic layer would help to maintain the pedestal height and width below the magnetohydrodynamic (MHD) stability thresholds for ELMs, thus causing mitigation and/or suppression [7].

Further studies, however, have demonstrated the importance of including the response of the plasma to the magnetic perturbations in order to understand properly the nature of mitigation and suppression of ELMs. Experimentally, the observation that the electron temperature gradient is typically unaffected by the application of magnetic perturbations is inconsistent with the idea of a stochastic pedestal [8]. Furthermore, the magnetic pitch of the applied perturbations has been varied in DIII-D [9] and ASDEX Upgrade [10] by continuously varying the toroidal phasing (or differential phase angle) between vertically separated rows of coils. It has been observed that the maximum mitigation or suppression of ELMs occurred at phasings different from the value at which the perturbed vacuum field was maximally resonant with the equilibrium magnetic field in the pedestal region. Subsequent MHD modeling has demonstrated that these optimal phasings are often well correlated with the total resonant perturbation, including vacuum and plasma response magnetic fields [9, 11–13].

Indeed, MHD theory predicts that the plasma response should have profound effects on the spectrum of magnetic perturbations. While ideal MHD requires that the resonant vacuum fields be completely screened by induced plasma currents at rational surfaces, resistivity permits the resonant fields to penetrate or even to be enhanced by tearing. Furthermore, non-resonant fields can excite kink-like deformations that can induce their own transport [14] and/or couple to resonant tearing modes to alter the behavior of ELM mitigation. Rotation profiles can also have a significant impact on the plasma response. In particular, strong, single-fluid toroidal rotation (or electron perpendicular rotation in two-fluid MHD) at a rational surface is capable of screening resonant perturbations, causing a resistive plasma to behave more ideally.

Recent experiments have suggested that magnetic-perturbation-induced ELM suppression is caused by the formation of an island at the top of the pedestal. Careful analysis of the bifurcation into and out of ELM suppression on DIII-D has shown an abrupt shift in the electron perpendicular rotation profile, such that the zero-crossing aligns with a rational surface at the pedestal top [15]. Linear, two-fluid M3D-C1 modeling has shown that this shift causes an increase in the resonant field at that surface, indicating that there is larger tearing drive for island formation at the pedestal top [16]. In this paradigm, ELM suppression is achieved by this island's arresting the growth of the pedestal height and width, preventing an ELM stability threshold from being crossed [17].

A proper test of this hypothesis will eventually require a comprehensive model that can predict the evolution of the pedestal across an ELM-suppression bifurcation. This will include time-dependent, nonlinear, two-fluid MHD simulations and an appropriate transport model, particularly for the momentum. Nevertheless, we can still pursue research on individual components of the model. Here, in order to form a better understanding of the effect that the rotation profile has on both the resonant and non-resonant plasma response to magnetic perturbations, we present results from linear, single-fluid, time-independent M3D-C1 plasma response calculations as the rotation profile is varied in an equilibrium reconstruction of a DIII-D ELM-suppression experiment. While the effect of rotation has been considered in the literature previously [16, 18–24], this study is unique given, collectively, its focus on changes in local rotation profiles in the vicinity of the zero-crossing near the pedestal top, its detailed examination of the non-resonant plasma response and its systematic nature.

In section 2, we discuss the M3D-C1 code and equilibrium in more detail. We also introduce a model rotation profile that is designed to largely match the experimental $\mathbf{E} \times \mathbf{B}$ rotation, but allows for systematic variation of the zero-crossing of the rotation profile. In section 3, we quantitatively assess the effects of the location of the zero-crossing on the resonant and non-resonant plasma response at and between rational surfaces. We also investigate how the quasilinear torque induced by the plasma response could play a role in ELM suppression and how the variations in plasma response could be detected by tokamak diagnostics. Finally, in section 4, we review this current work and discuss future work needed to understand these results more fully and to extend them.

2. Methods

The M3D-C1 code [25] solves the three-dimensional extended MHD equations including two-fluid effects and dissipative terms (i.e., resistivity, particle diffusivity, viscosity and thermal conductivity). It uses a high-order finite element representation in a cylindrical (R, φ, Z) coordinate system, where R is the major radius, φ is the toroidal angle and Z is the height, allowing for simulation of the bulk plasma, the scrape-off layer and the highly resistive, vacuum-like open-field-line region (OFLR). In addition to this plasma region, in which the MHD equations are solved, the M3D-C1 simulation domain contains a finite-thickness resistive wall and an external vacuum region, in which appropriate equations for those regimes are solved [26]. In this study, we focus on single-fluid, time-independent linear simulations. The plasma is taken to have uniform, isotropic particle diffusivity and

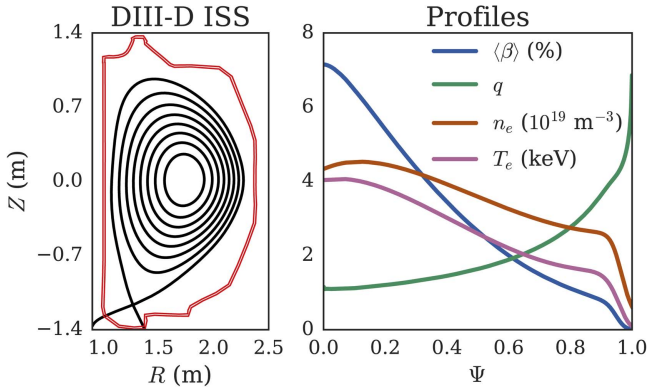

Figure 1. EFIT reconstruction of DIII-D shot 158103 at 3796 ms. Left: flux surfaces (black) and resistive wall (red). Right: flux-surface-averaged plasma β (i.e., the ratio of the local thermal pressure to the local magnetic pressure), safety factor q, electron density n_e and electron temperature T_e.

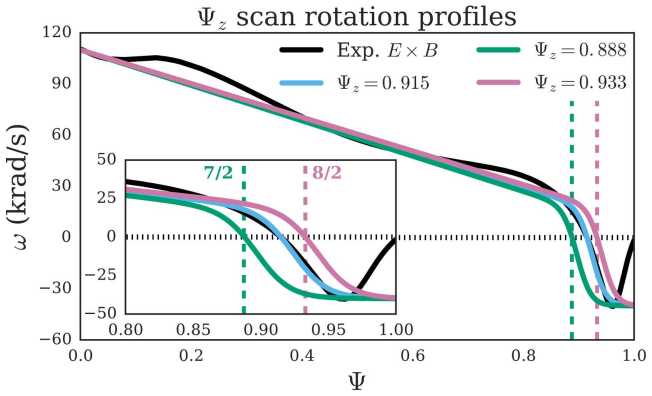

Figure 2. Experimental $\mathbf{E} \times \mathbf{B}$ toroidal rotation profile for DIII-D shot 158103 at 3796 ms along with three model rotation profiles using equation (1). All have $\omega_0 = 110$ krad s^{-1}, $\omega_\infty = -40$ krad s^{-1}, $\Psi_c = \Psi_z + 0.01$ and $\Delta\Psi = 0.025$, while Ψ_z is varied. The curve with $\Psi_z = 0.915$ is a good match to the experimental rotation profile, while the other two are chosen to have Ψ_z coincide with a rational surface, namely $q = 7/2$ at $\Psi = 0.888$ and $q = 8/2$ at $\Psi = 0.933$ (each denoted by dashed lines). The insert zooms in on the edge region. The dotted line denotes $\omega = 0$.

kinematic viscosity, while the thermal conductivities are spatially uniform but anisotropic, with a parallel conductivity 10^6 times the perpendicular value. The resistivity is assumed to be Spitzer, varying as $T_e^{-3/2}$. While the resistive wall plays no dynamic role in these stationary solutions, it is included to allow for free-boundary-like calculations with the superconducting boundary condition placed far from the plasma (in these cases, outside the poloidal field coils).

M3D-C1 typically takes an experimental equilibrium reconstruction as an input. In particular, the pressure, p, and toroidal field function, F, profiles are read from the reconstruction and the equilibrium is recomputed by M3D-C1's Grad–Shafranov solver. In simulations where the domain extends beyond the poloidal field coils, such as those presented here, the coil currents are taken as inputs and then iterated upon until a good shape match to the original equilibrium is achieved. The electron density, n_e, electron temperature, T_e, and toroidal rotation, ω, profiles are also input parameters. While they do not affect the Grad–Shafranov equilibrium, these profiles are used in the linear calculations. Furthermore, n_e, T_e, and p are all extrapolated to small values in the OFLR to ensure that this region exhibits vacuum-like behavior.

The simulations presented here are based upon an EFIT [27–29] reconstruction of DIII-D shot 158103 at 3796 ms. This is the 'reference' equilibrium considered in recent multimode plasma response studies [9, 30], which is an ITER-similar shape (ISS) lower single null plasma with normalized beta $\beta_N \approx 2.2$, pedestal-top electron collisionality $\nu_e^* \approx 0.30$ and edge safety factor $q_{95} \approx 4.15$ (see figure 1). Given the assumptions of our dissipation models, the magnetic Prandtl number is $Pr_m \sim \mathcal{O}(10^2)$ and the Lundquist number is $S \sim \mathcal{O}(10^8)$ at the pedestal top. In the experiment, toroidal mode number $n = 2$ magnetic perturbations were applied using the in-vessel I-coils. Each row of coils carried approximately 4 kA of current and the phasing $\Delta\phi_{UL}$ between the upper (IU) and lower (IL) I-coils was varied throughout the experiment. ELM suppression was achieved in a narrow phasing range from $\Delta\phi_{UL} \approx 0°–45°$. The equilibrium considered here was taken during a non-suppressed period, as we wish to investigate the role of the rotation profile in determining plasma response and bifurcation into ELM suppression.

In this study, we consider single-fluid simulations that use the n_e and T_e profiles taken from the experiment (extended into the OFLR). All simulations consider vacuum 3D fields produced by idealized, $n = 2$ Fourier-mode currents at the location of IU and IL. The toroidal rotation profile is taken to be a free function of the normalized poloidal flux, Ψ. In particular, we will use a model rotation profile of the form

$$\omega(\Psi) = \frac{1}{2}(\omega_0 - \omega_\infty - h\Psi)\,\Theta(\Psi) + \omega_\infty, \tag{1}$$

where

$$\Theta(\Psi) = 1 - \tanh\left(\frac{\Psi - \Psi_c}{\Delta\Psi}\right) \tag{2}$$

and

$$h = \frac{1}{\Psi_z}\left(\omega_0 - \omega_\infty + 2\frac{\omega_\infty}{\Theta(\Psi_z)}\right). \tag{3}$$

This rotation profile has five free parameters: the on-axis rotation, ω_0, the asymptotic rotation as $\Psi \to \infty$, ω_∞, the zero-crossing of the rotation profile, Ψ_z, and the center and width of the hyperbolic tangent, Ψ_c and $\Delta\Psi$, respectively. Using $\omega_0 = 110$ krad s^{-1}, $\omega_\infty = -40$ krad s^{-1}, $\Psi_z = 0.915$ and $\Delta\Psi = 0.025$, we can match the experimental $\mathbf{E} \times \mathbf{B}$ rotation profile well, as seen in figure 2. The location of greatest difference is at the very edge ($\Psi > 0.97$), but the experimental rotation profile is relatively poorly constrained in this region anyway. By modifying the free parameters from these values, we are able to vary quantities of interest (e.g., the rotation and rotation shear at a specific Ψ) while maintaining an otherwise experimentally relevant rotation profile.

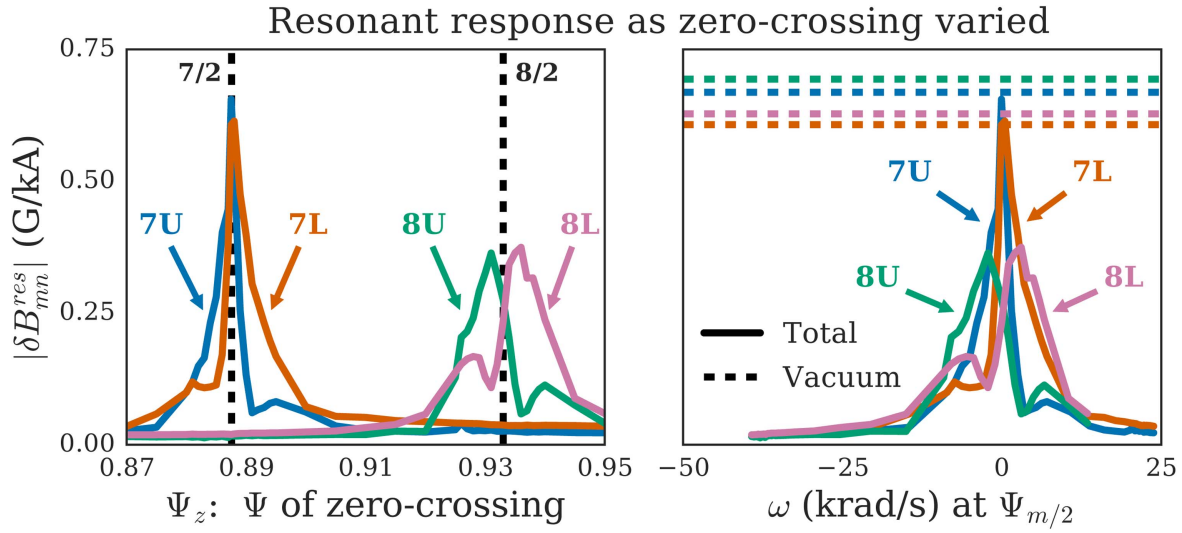

Figure 3. Magnitude of the resonant field induced by the upper and lower I-coils at $q = 7/2$ and $q = 8/2$ in the equilibrium of figure 1 for rotation profiles defined by equation (1) with $\omega_0 = 110$ krad s^{-1}, $\omega_\infty = -40$ krad s^{-1}, $\Psi_c = \Psi_z + 0.01$ and $\Delta\Psi = 0.025$, and varying Ψ_z. These are plotted both versus Ψ_z (left) and versus ω at the relevant rational surface (right). Each curve is labeled by the negative of its m number, 7 or 8, along with its coil, upper (U) or lower (L). The locations of the two rational surfaces are denoted by the dotted lines in the left-hand plot. Total field includes both the vacuum field and plasma response.

3. Results

Previous simulations have found [19, 21, 22, 26, 31] and experiments have suggested [15, 16] that a zero-crossing of the rotation profile (or electron perpendicular rotation profile in two-fluid MHD) at a rational surface permits penetration of resonant fields, while strong rotation at the surface screens resonant fields. In order to quantify this more carefully, we perform a systematic scan of the zero-crossing using the model rotation profile of equation (1). We take the same ω_0, ω_∞ and $\Delta\Psi$ for the experimentally matched rotation profile noted in section 2 and vary Ψ_z from 0.87 to 0.95, while keeping $\Psi_c = \Psi_z + 0.01$. Two such model rotation profiles are shown in figure 2, one passing through zero at the $\Psi = 0.888 \approx \Psi_{7/2}$ and the other at $\Psi = 0.933 \approx \Psi_{8/2}$. Here, we have defined $\Psi_{m/n}$ as the normalized poloidal flux location of the $q = m/n$ surface, where q is the safety factor and m is the poloidal mode number. Note that the rotation profile is largely fixed outside the vicinity of the zero-crossing.

To examine the effects of the rotation profile on the plasma response, we will consider a Fourier decomposition of $\delta\mathbf{B}$, the perturbed magnetic field. In particular, the radial perturbed field can be decomposed as

$$\delta B_{mn}(\Psi) = \frac{(2\pi)^2}{A} \iint \frac{\delta\mathbf{B}\cdot\nabla\psi}{\mathbf{B}\cdot\nabla\theta} e^{i(m\theta - n\varphi)} d\theta d\varphi, \qquad (4)$$

where A is the area of the flux surface and $\mathbf{B}$ is the equilibrium, axisymmetric magnetic field. The integral is taken in straight-field-line coordinates (ψ, θ, φ), where ψ is the poloidal flux over 2π and θ is the poloidal angle.

3.1. Resonant response

The magnitude of the resonant magnetic field at $\Psi_{7/2}$ and $\Psi_{8/2}$ as Ψ_z is varied is shown in figure 3, where the resonant field is defined as

$$\delta B^{res}_{mn} = \delta B_{mn}(\Psi_{m/n}). \qquad (5)$$

We include only these responses as the rotation at any other rational surface is nearly constant throughout the scan and the change in the resonant response there is negligible. In addition, the responses for upper and lower I-coils are shown separately because the constructive or destructive interference of the IU and IL responses would introduce the phasing as a complicating variable in this analysis.

As the zero-crossing passes through a rational surface, the resonant response at that surface generally peaks. The upper and lower I-coil responses, however, have two distinct peaks of different magnitudes. At the $q = 7/2$ surface, the larger peak lies where $\Psi_z = \Psi_{7/2}$ for both IU and IL. Each curve, however, is weighted to either side of the rational surface, with the IU response (labeled 7U) skewed toward $\Psi_z < \Psi_{7/2}$ and the IL response (labeled 7L) toward $\Psi_z > \Psi_{7/2}$. A much smaller peak occurs on the lesser-weighted side. This effect is even more prominent for the resonant field at the $q = 8/2$ surface, with two distinct peaks on either side of $\Psi_{8/2}$ that differ in magnitude by a factor of two to three. A similar weighting to either side of the surface is observed, with the $\Psi_z < \Psi_{8/2}$ response greater for IU (labeled 8U) and $\Psi_z > \Psi_{8/2}$ for IL (labeled 8L).

Figure 3 also shows these same resonant responses plotted against the ω at the relevant rational surface, as computed from the M3D-C1 equilibrium. Clearly, the resonant response peaks for low values of rotation, roughly $|\omega| \lesssim 5$ krad s^{-1}, but the weightings and double peaks still exist, with the IU responses (7U and 8U) skewed toward negative rotation and the IL responses (7L and 8L) toward positive rotation. Note that the vacuum levels of the resonant magnetic fields (i.e. the perturbation field without plasma response) are also shown in figure 3, indicating that for these

rotation profiles the plasma response at least partially screens the vacuum field for all but the very lowest rotation at $\Psi_z = \Psi_{7/2}$.

The cause of the two peaks is uncertain. One possibility is that multiple distinct modes are being driven in the vicinity of the rational surface that could constructively or destructively interfere with each other. The phase of these modes would change depending on which coil was driving them, possibly leading to the differing behavior between the IU and IL responses. Another possibility is that distinct resonances are being crossed that don't necessarily align directly on the rational surface. For example, Alfvén splitting results in two resonant surfaces forming on either side of a rational surface, one caused by a rotational resonance with the shear Alfvén wave and the other with the sound wave. Previous demonstration of this effect, however, found it only in the limit of fast toroidal flow [32], so the applicability of the theory to this case with a nearby zero-crossing is unclear. Lastly, the Glasser–Greene–Johnson (GGJ) effect [33] has been shown to provide a source of resonant field screening at low rotation [24]. This could explain why the peak resonant response at the $q = 4$ surface does not occur for zero rotation there. This same effect, however, is not seen at the $q = 7/2$ surface, possibly due to the lower pressure gradient there. That said, it is not clear how the GGJ effect would not explain asymmetry between the IU and IL responses or between positive and negative rotation. Further research is needed to determine fully the cause of these peaks.

3.2. Non-resonant response

The effect of the zero-crossing is not restricted to the resonant response as there is broad coupling of the poloidal Fourier harmonics in the direct vicinity of Ψ_z. This is true even if the zero-crossing is far from a resonant surface. δB_{mn} is plotted in figure 4 for $\Psi_z \approx \Psi_{7/2}$, $\Psi_z = 0.915$ (i.e. between $\Psi_{7/2}$ and $\Psi_{8/2}$) and $\Psi_z \approx \Psi_{8/2}$. In all three cases, a pronounced streak across m is observed on the left-hand plots in the region around $|\Psi - \Psi_z| \lesssim 0.01$. The plots of δB_{mn} versus Ψ for multiple m values on the right-hand side make it clear that there is local peaking of the near-resonant harmonics (i.e. $|m - nq| \lesssim 2$) at Ψ_z, while the far-off-resonant harmonics (i.e. $|m - nq| \gtrsim 2$) are reduced.

This modification of the magnetic field is coincident with a local perturbed current density, $\delta\mathbf{J}$, in the vicinity of Ψ_z. Figure 5 shows the Fourier decomposition of the perturbed parallel current density for $\Psi_z = 0.915$ between rational surfaces and $\Psi_z = 0.933$ coincident with the $q = 8/2$ surface. Here, we define

$$\delta J_{mn}(\Psi) = \frac{(2\pi)^2}{A} \iint \frac{R\delta\mathbf{J}\cdot\mathbf{B}}{\mathbf{B}\cdot\nabla\theta} e^{i(m\theta - n\varphi)} d\theta d\varphi. \quad (6)$$

It is clear that in each case, the current density is localized to the near-resonant harmonics. While the resonant field is undoubtedly impacted by this resonant current in the case of for $\Psi_z = 0.933$, the current density at $\Psi_z = 0.915$ is not near an $n = 2$ rational surface and has a broader m spectrum. Thus, this non-resonant current cannot be related to a tearing response.

In order to assess the nature of this off-rational perturbed current, we performed a scan of the shear at $\Psi_z = 0.915$ by varying $\Delta\Psi$ from 6.25×10^{-3} to 1×10^{-1}, bracketing the experimentally matching value of $\Delta\Psi = 2.5 \times 10^{-2}$ used in the Ψ_z scan. The flux surface average of the perturbed toroidal current density is shown for the various shear values in figure 6. From this, it is clear that increasing rotation shear leads to an increased plasma response in the vicinity of Ψ_z, indicating that shear has an amplifying effect on whatever non-resonant mode or modes are being driven by the field here. The response is not directly proportional to the shear, however, and seems to require the crossing of a threshold to appear, as suggested by the rapid five-fold increase in the current from $d\omega/d\Psi = -564$ krad s^{-1} to -1058 krad s^{-1}. While the exact nature of this response remains unclear from this analysis, this current must be necessary for restoring force balance in these non-axisymmetric equilibria with three-dimensionally perturbed pressures and magnetic fields.

3.3. Quasilinear torque

Thus far we have considered the effect that the rotation profile has on the plasma response. It is natural to consider how this plasma response would then, in turn, feed back on the rotation through the quasilinear electromagnetic torque density, defined as

$$\tau(\Psi) = \langle R^2 \nabla\varphi \cdot (\delta\mathbf{J} \times \delta\mathbf{B}) \rangle, \quad (7)$$

where $\langle \cdots \rangle$ denotes a flux surface average. In figure 7, we have plotted this torque versus Ψ and each Ψ_z of the zero-crossing scan of figure 3. For zero-crossings that are not in the vicinity of a rational surface, the pronounced non-resonant response presented in section 3.2 produces a large torque density localized near Ψ_z. The significant negative torque for $\Psi < \Psi_z$ and positive torque for $\Psi > \Psi_z$ will act to flatten the negative gradient of the rotation profile near the zero-crossing. By reducing the shear, the quasilinear torque will act to suppress the non-resonant mode that is driving it. In addition, the reduced rotation shear could destabilize turbulent modes in the vicinity of the zero-crossing, providing a possible mechanism for the limitation of pedestal growth in the presence applied 3D magnetic perturbations.

The torque profiles in figure 7 change significantly when the zero-crossing is in the vicinity of a rational surface (i.e. when there is a significant resonant response). In particular, there appear to be regions of low torque density with adjacent regions of particular high torque density. This indicates that there may exist rotation profiles with $\Psi_z \approx \Psi_{m/2}$ that are relatively stable compared with the rotation profiles with zero-crossings between rational surfaces that the quasilinear torque tends to flatten. As experiments suggest that the zero-crossing of the (electron perpendicular) rotation tends to align with a rational surface upon a bifurcation into ELM suppression [15], the effect of the quasilinear electromagnetic torque on the location of the zero-crossing is of particular interest. As negative torque will produce negative rotation at that Ψ

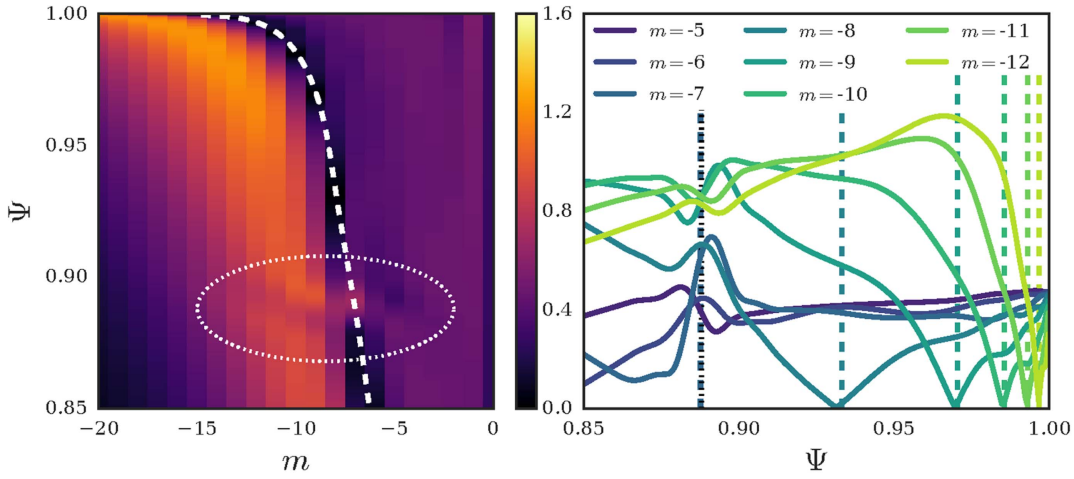

(a) δB_{mn} (G/kA) for $\Psi_z = 0.888 \approx \Psi_{7/2}$

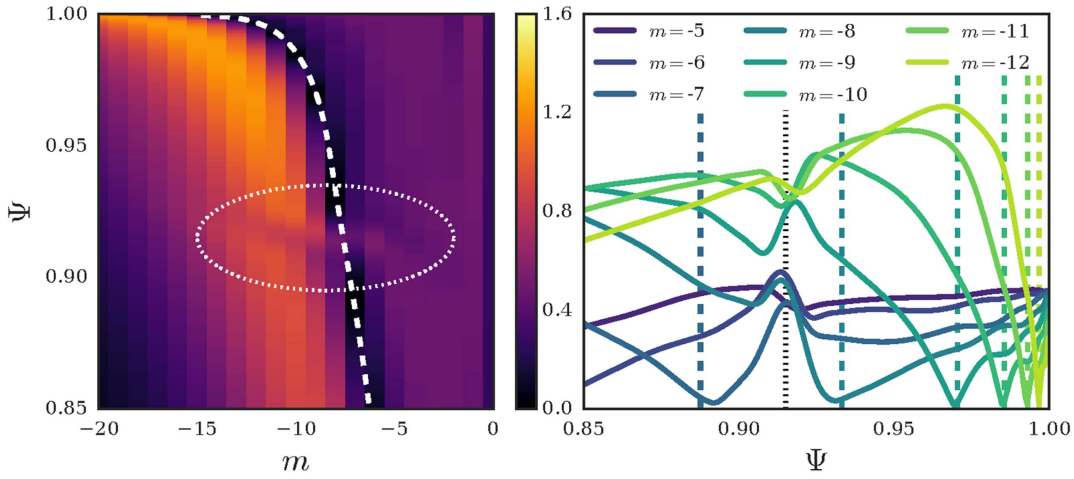

(b) δB_{mn} (G/kA) for $\Psi_z = 0.915$

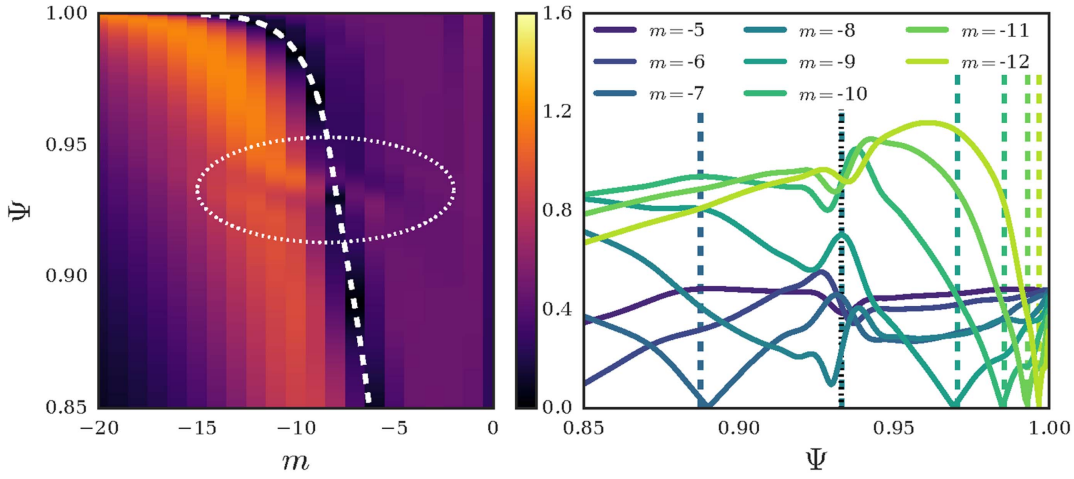

(c) δB_{mn} (G/kA) for $\Psi_z = 0.933 \approx \Psi_{8/2}$

Figure 4. Fourier decomposition of the total perturbed magnetic field for IL with the rotation profile used in the Ψ_z scan for various Ψ_z. Left: δB_{mn} versus the poloidal mode number m and normalized flux Ψ. The resonant $m = nq$ line is in dashed white. The streak circled in dotted white is centered about Ψ_z. Right: individual poloidal harmonics versus Ψ. The Ψ location for the respective $q = m/n$ locations are indicated with dashed lines, while the Ψ_z location is denoted in dotted black and overlaps a rational q line in (a) and (c). The color bar on the left and the y-axis on the right share the same values.

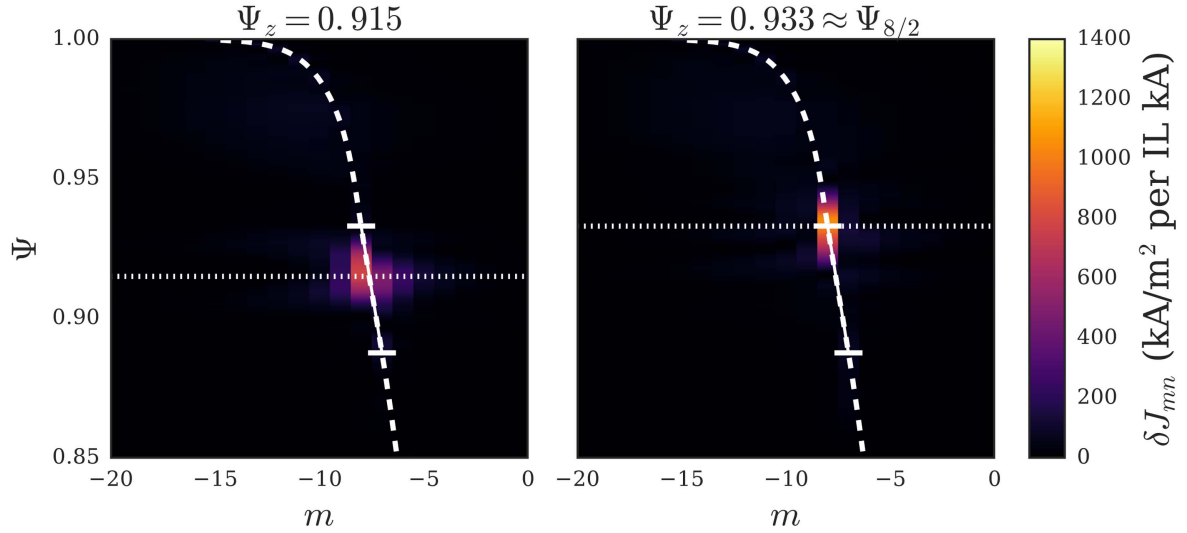

Figure 5. Fourier decomposition of the perturbed parallel current in response to IL versus the poloidal mode number m and normalized flux Ψ for a rotation zero-crossing between rational surfaces (left) and coincident with a rational surface (right). The resonant $m = nq$ line is in dashed white, with horizontal white ticks denoting the $q = 7/2$ and $q = 8/2$ surfaces.

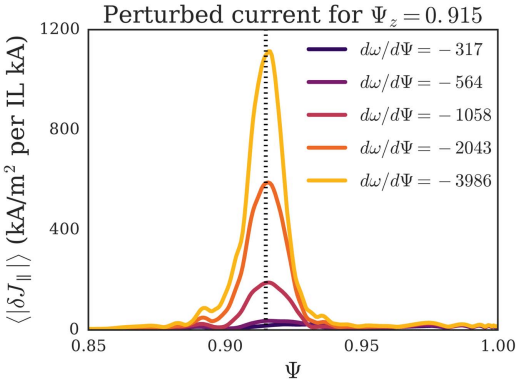

Figure 6. Flux surface average of the magnitude of the perturbed parallel current density caused by the plasma response to IL for rotation profiles defined by equation (1) with $\omega_0 = 110$ krad s^{-1}, $\omega_\infty = -40$ krad s^{-1}, $\Psi_z = 0.915$ (marked in dashed black), $\Psi_c = \Psi_z + 0.4\Delta\Psi$ and varying $\Delta\Psi$. The legend denotes the rotation shear at Ψ_z in krad s^{-1}.

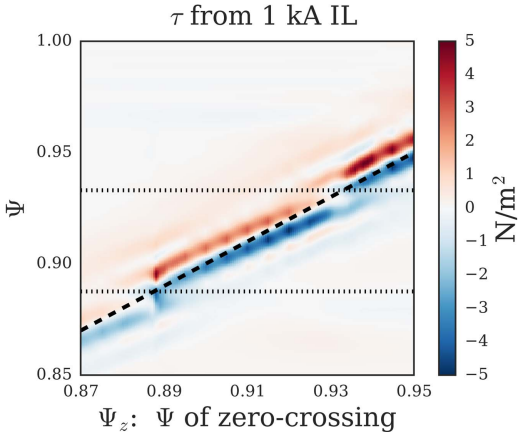

Figure 7. The quasilinear electromagnetic torque caused by the plasma response to IL with 1 kA of current for rotation profiles used in the Ψ_z scan versus both the zero-crossing location and Ψ. The dashed line denotes $\Psi = \Psi_z$ and the dotted lines denote the $q = 7/2$ (lower) and $q = 8/2$ (upper) rational surfaces.

location, driving the zero-crossing inward, and vice versa for positive rotation, there will exist stable points of the zero-crossing when

$$\tau(\Psi_z) = 0 \quad \text{and} \quad \frac{d\tau}{d\Psi_z}(\Psi_z) < 0. \tag{8}$$

Figure 8 shows the value of τ at Ψ_z for each rotation profile in the zero-crossing scan. We can identify two stable points in the IL-induced torque, one just inside each rational surface, and one stable point in the IU-induced torque at the $q = 7/2$ surface. For most values of Ψ_z, the torque density is negative, driving the zero-crossing inward toward a stable point. For the small regions of positive torque density just inside the stable points, however, the drive would be outward. Regardless, the quasilinear torque density clearly provides a drive of the zero-crossing toward the vicinity of a rational surface. While this quasilinear electromagnetic torque must compete with other sources of torque in the plasma (e.g.,

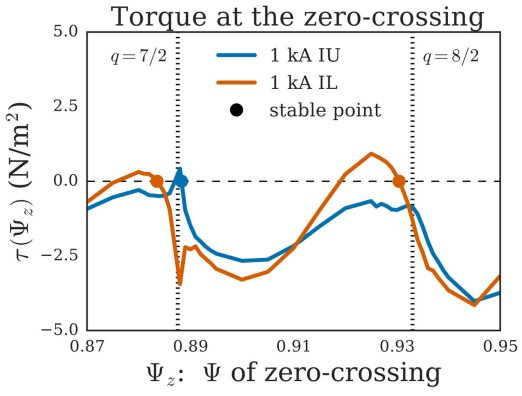

Figure 8. The quasilinear electromagnetic torque at the location of the zero-crossing for the rotation profiles used in the Ψ_z scan. The torques induced by the upper and lower I-coils are shown separately. The dashed lines denote where Ψ_z is coincident with a rational surfaces.

quasilinear Reynolds stress, neutral beams, neoclassical toroidal viscosity), it is a promising mechanism for the observed evolution of the rotation profile during the ELM-suppression bifurcation.

Finally, we note that non-resonant torque in the vicinity of the zero-crossing is unexpected based on conventional MHD studies. Typically, it is assumed that the plasma has an ideal response outside the narrow resistive layer around a rational surface, therefore allowing for quasilinear torque at the rational surfaces but not in between [34, 35]. The present case, however, seems sufficiently different from the assumptions of previous studies to permit the torque profiles in figure 7. Firstly, we would not expect to see significant resonant torque when the zero-crossing lies between the rational surfaces, since the resonant response is well screened. Furthermore, the single-fluid M3D-C1 model goes beyond standard resistive MHD to include particle diffusivity, kinematic viscosity and thermal conductivity. These additional dissipation terms may provide drive for these non-resonant modes between the rational surfaces. In addition, even within the resistive MHD model, the small equilibrium rotation may create a non-ideal region around the zero-crossing, as can be seen from the linearized Faraday's law:

$$\frac{\partial \delta \mathbf{B}}{\partial t} + in\omega\delta\mathbf{B} = R^2(\delta\mathbf{B}\cdot\nabla\omega)\nabla\varphi + \nabla\times(\delta\mathbf{v}\times\mathbf{B}) - \nabla\times(\delta\eta\mathbf{J} + \eta\delta\mathbf{J}), \tag{9}$$

where $\delta\mathbf{v}$ is the perturbed velocity and η and $\delta\eta$ are the equilibrium and perturbed resisitivity, respectively. In steady state and in a region where ω is sufficiently small, the $\nabla\psi$ projection of this equation requires that the $\delta\mathbf{v}\times\mathbf{B}$ term be balanced by the resistive terms. Such a non-ideal region could permit the non-resonant currents and torque densities presented here. Further work, however, is required to determine the origin of these non-resonant modes with greater certainty.

3.4. Observability

Given the significant variation in both the resonant and non-resonant plasma response, it is important to investigate how this behavior affects quantities that are observable by external measurements. One of the most commonly used diagnostics on DIII-D for 3D field experiments is a magnetic sensor array capable of measuring the magnetic field induced by low-n plasma perturbations [36]. In particular, the magnetic signals on the low-field side (LFS) and high-field side (HFS) midplane have been used to demonstrate that the $n = 2$ plasma response is a combination of multiple modes being simultaneously driven in the plasma [9, 30] as well as to provide significant insight into the nature of the ELM-suppression bifurcation [15].

In figure 9, we have plotted the magnitude and phase of the perturbed plasma magnetic field (i.e. the total field minus the vacuum field) induced by IU and IL at the LFS and HFS midplane probes as the zero-crossing of the rotation profile is varied, as in the zero-crossing scan of figure 3. On the HFS,

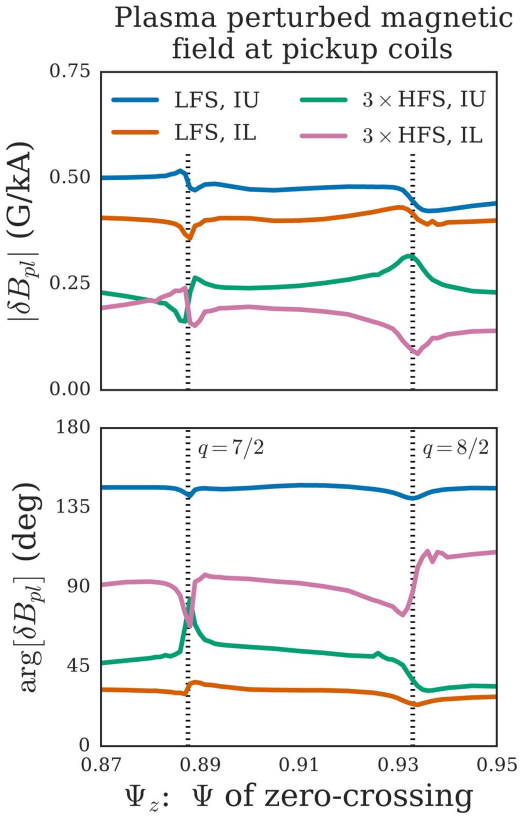

Figure 9. The magnitude and phase of the perturbed magnetic field at the high-field side (magnitude times three) and low-field side midplane magnetic sensors on DIII-D versus the location of the zero-crossing for the rotation profiles used in the Ψ_z scan. The field shown is only the plasma response (total minus vacuum field) to IU and IL, separately. The locations of the $q = 7/2$ and $q = 8/2$ rational surfaces are denoted by the dotted lines.

the magnitude varies by $\pm 33\%$ throughout the scan, changing most significantly when Ψ_z is near a rational surface (i.e. when there is a significant resonant response). In addition, there is a significant change in the phase of the HFS response for Ψ_z near a rational surface. The phase shift near $q = 7/2$ occurs only when the zero-crossing is in the vicinity of that resonant surface, indicating that the shift is due to the enhanced resonant response there. The shift near $\Psi_z = \Psi_{8/2}$, however, results in a distinct phase difference between the HFS response with $\Psi_z < \Psi_{8/2}$ and $\Psi_z > \Psi_{8/2}$. Though seemingly related to physics at the rational surface, the shift can't be solely caused by the resonant response there. This is most readily seen by the fact that the resonant responses are comparable for $\Psi_z = 0.92$ and $\Psi_z = 0.95$ (see figure 3), but the HFS phases for these two zero-crossings are significantly different. As the other resonant responses are largely unchanged throughout this range of Ψ_z, this phase shift should be caused by a change in phase of the non-resonant plasma response for zero-crossings on either side of the $q = 8/2$ surface. It may be possible to distinguish between resonant and non-resonant effects by considering the magnitude of the response; while both changes in plasma response induce a phase shift, only changes to the resonant response significantly affect the magnitude of the HFS perturbed magnetic

field. In comparison with these rather robust changes in the HFS signal, the magnitude of the LFS signal varies by only $\pm 10\%$ throughout the Ψ_z scan and the LFS phase is essentially constant. Thus, we can conclude that the HFS magnetic sensors on DIII-D should be capable of detecting changes to the plasma response caused by shifts in the rotation zero-crossing around rational surfaces, while the LFS sensors should be largely insensitive to these effects.

Another effect commonly observed in 3D field experiments is the splitting of divertor strike points due to the creation of homoclinic tangles [37, 38]. On DIII-D, this can be measured using high-speed cameras directed toward the lower divertor. In particular, cameras equipped with carbon-III line filters have shown that the degree of strike point splitting is greater during periods of ELM suppression than during ELMing periods with comparable applied 3D fields. In order to assess how the strike point structure should change as the zero-crossing of the rotation profile is varied, we have calculated the divertor footprint structure with the TRIP3D-MAFOT code [39] for several of the M3D-C1 runs used in the zero-crossing scan of figure 3. These simulations confirm that the island width at the $q = m/2$ surface increases when Ψ_z is in the vicinity of $\Psi_{m/2}$, as required by the increased resonant response there. Nevertheless, for the 4 kA I-coil currents applied in the experiment from which our equilibrium was reconstructed, the calculated islands remain small enough that they fail to increase stochasticization in the edge. Thus, the increased resonant response when Ψ_z is near a rational surface has little impact on the size and phase of divertor footprints. Likewise, the change in location of non-resonant modes near the zero-crossing did not substantially affect the footprints. We conclude, therefore, that the zero-crossing-induced plasma responses computed here should not have an observable effect on strike point splitting.

4. Conclusion

A systematic scan of the zero-crossing of the single-fluid rotation profile in M3D-C1 linear, time-independent plasma response calculations has been performed for a typical DIII-D ITER-similar shape reconstructed equilibrium. In general, it was found that low rotation near a rational surface permitted the penetration of resonant magnetic fields. Multiple peaks in the profiles of $|\delta B_{mn}^{\mathrm{res}}|$ for both the upper and lower I-coils indicate that multiple resonances may exist in the vicinity of a rational surface and complicate the idea that a zero-crossing directly coincident with a rational surface is necessary for significant tearing drive. Furthermore, we observed that the zero-crossing has significant effects on the plasma response even when Ψ_z is far from a rational surface. In particular, we have shown that there is an amplification of near-resonant (though still non-resonant) Fourier harmonics of the perturbed magnetic field near Ψ_z, while the far-off-resonant harmonics are reduced. This broad coupling across magnetic Fourier modes is induced by a perturbed current density centered about Ψ_z. A shear scan for the case where the zero-crossing was in between two rational surfaces indicates that this non-resonant response is amplified by significant shear at Ψ_z, although the exact nature of the mode or modes being driven is unclear. Collectively, these results demonstrate that single-fluid plasma response calculations can be highly sensitive to the details of the rotation profile, particularly in the neighborhood of a zero-crossing. When performing such simulations, careful attention should be paid to this rotation profile in order to ensure that the phenomena of interest are computed with high fidelity.

An analysis of the quasilinear torque density allowed us to hypothesize that the non-resonant plasma response could play an important role in ELM-suppression dynamics through two effects. First, the non-resonant response induced a torque that would flatten the rotation profile in the vicinity of the zero-crossing. The reduced rotation shear may destabilize turbulent modes, increasing transport and arresting the growth of the pedestal height and width. Second, this torque would drive the rotation zero-crossing toward particular stable points in the vicinity of a rational surface, allowing for an increased resonant response there and possible island penetration.

Finally, by considering some of the commonly used diagnostics in 3D field experiments, we were able to show that increases in the resonant response should be detectable by a change in both amplitude and phase of the perturbed magnetic field on the high-field side of a tokamak. Changes in the location of the non-resonant response, however, did not appear to produce measurable changes in magnetic signals outside of the plasma. Furthermore, calculations performed with the TRIP3D-MAFOT code for these M3D-C1 results revealed that variation of neither the resonant nor the non-resonant responses described here produced a detectable change to the divertor footprint structure.

Significant work remains in order to understand these results more fully, to extend the results and to apply this research directly to ELM-suppression studies. Additional numerical zero-crossing scans at different rotation shear values would allow for the investigation of how the non-resonant, shear-amplified response interacts with the resonances at or near rational surfaces. It is possible that the differing behavior between the IU and IL responses shown here could be due to varying coupling between the resonant, tearing response and the non-resonant, shear-amplified response. In addition, modifying the edge of our model rotation profile to approach zero near $\Psi = 1$, as in the experimental $\mathbf{E} \times \mathbf{B}$ rotation profile, would allow us to understand how significant resonant response near the separatrix impacts the plasma response in the pedestal region, as well as the observable magnetic signals and divertor footprints. Further research ought to be done into the nature of the non-resonant response as well, in order to assess what modes are being driven in the plasma and to determine if this response is, at least in part, responsible for bifurcations into ELM suppression. Quasilinear and nonlinear simulations would provide necessary insight into the evolution of the rotation profile due to the plasma response, along with the saturation level of the resonant and non-resonant responses.

Finally, two-fluid simulations are required for increased applicability to experimental analysis. The most relevant

additional physics in such calculations would be the inclusion of separate ion and electron rotation profiles. The electron rotation profile generally has similar qualitative features to the single-fluid rotation we have modeled here. Based on known theory [17, 40] and computational experience [22, 26], we expect that the effect of the rotation zero-crossing on the resonant field presented here should qualitatively extend to the electron rotation's zero-crossing in two-fluid simulations. It is uncertain, however, to which rotation the non-resonant plasma response, and thus the quasilinear torque, would be sensitive. The M3D-C1 code and the flexible, parameterized rotation model presented here should remain valuable tools throughout all this ongoing work.

Acknowledgments

This research was supported by the US Department of Energy Fusion Energy Sciences Postdoctoral Research Program administered by the Oak Ridge Institute for Science and Education (ORISE) for the DOE. ORISE is managed by Oak Ridge Associated Universities (ORAU) under DOE contract no. DE-AC05-06OR23100. All opinions expressed in this paper are the authors' and do not necessarily reflect the policies and views of DOE, ORAU or ORISE. This work was sponsored in part by the US Department of Energy under grant nos DE-FG02-95ER54309 and DE-FC02-06ER54873 and the SciDAC Center for Extended Magnetohydrodynamic Modeling (CEMM).

References

[1] Evans T *et al* 2006 *Nat. Phys.* **2** 419
[2] Liang Y *et al* 2007 *Phys. Rev. Lett.* **98** 265004
[3] Suttrop W *et al* 2011 *Phys. Rev. Lett.* **106** 225004
[4] Jeon Y M *et al* 2012 *Phys. Rev. Lett.* **109** 035004
[5] Kirk A *et al* 2013 *Nucl. Fusion* **53** 043007
[6] Sun Y *et al* 2016 *Phys. Rev. Lett.* **117** 115001
[7] Fenstermacher M E *et al* 2008 *Phys. Plasmas* **15** 056122
[8] Evans T *et al* 2004 *Phys. Rev. Lett.* **92** 235003
[9] Paz-Soldan C *et al* 2015 *Phys. Rev. Lett.* **114** 105001
[10] Suttrop W, Barrera Orte L, Fischer R, Fietz S, Fuchs J, McDermott R, Rathgeber S, Viezzer E and Wolfrum E 2014 *XXV IAEA Fusion Energy Conf. (Saint Petersburg, Russia)* pp EX/P1–23
[11] Kirk A *et al* 2015 *Nucl. Fusion* **55** 043011
[12] Liu Y *et al* 2016 *Nucl. Fusion* **56** 056015
[13] Orain F *et al* 2017 *Nucl. Fusion* **57** 022013
[14] Callen J, Cole A and Hegna C 2012 *Phys. Plasmas* **19** 112505
[15] Nazikian R *et al* 2015 *Phys. Rev. Lett.* **114** 105002
[16] Wade M *et al* 2015 *Nucl. Fusion* **55** 023002
[17] Snyder P B, Osborne T H, Burrell K H, Groebner R J, Leonard A W, Nazikian R, Orlov D M, Schmitz O, Wade M R and Wilson H R 2012 *Phys. Plasmas* **19** 056115
[18] Izzo V and Joseph I 2008 *Nucl. Fusion* **48** 115004
[19] Liu Y, Kirk A and Nardon E 2010 *Phys. Plasmas* **17** 122502
[20] Liu Y, Kirk A, Gribov Y, Gryaznevich M, Hender T and Nardon E 2011 *Nucl. Fusion* **51** 083002
[21] Becoulet M *et al* 2012 *Nucl. Fusion* **52** 054003
[22] Ferraro N M 2012 *Phys. Plasmas* **19** 056105
[23] Liu Y, Ham C J, Kirk A, Li L, Loarte A, Ryan D A, Sun Y, Suttrop W, Yang X and Zhou L 2016 *Plasma Phys. Control. Fusion* **58** 114005
[24] Li L, Liu Y, Liang Y, Wang N, Luan Q, Zhong F and Liu Y 2016 *Nucl. Fusion* **56** 092008
[25] Jardin S C, Ferraro N, Breslau J and Chen J 2012 *Comput. Sci. Discovery* **5** 014002
[26] Ferraro N M, Jardin S C, Lao L L, Shephard M S and Zhang F 2016 *Phys. Plasmas* **23** 056114
[27] Lao L, St John H, Stambaugh R, Kellman A and Pfeiffer W 1985 *Nucl. Fusion* **25** 1611
[28] Lao L, Ferron J, Groebner R, Howl W, St John H, Strait E and Taylor T 1990 *Nucl. Fusion* **30** 1035
[29] Lao L, St John H, Peng Q, Ferron J R, Strait E J, Taylor T S, Meyer W H, Zhang C and You K I 2005 *Fusion Sci. Technol.* **48** 968
[30] Paz-Soldan C, Logan N, Haskey S, Nazikian R, Strait E, Chen X, Ferraro N, King J, Lyons B and Park J 2016 *Nucl. Fusion* **56** 056001
[31] Ferraro N, Evans T, Lao L, Moyer R, Nazikian R, Orlov D, Shafer M, Unterberg E, Wade M and Wingen A 2013 *Nucl. Fusion* **53** 073042
[32] Liu Y Q *et al* 2012 *Plasma Phys. Control. Fusion* **54** 124013
[33] Glasser A H, Greene J M and Johnson J L 1975 *Phys. Fluids* **18** 875
[34] Fitzpatrick R 1993 *Nucl. Fusion* **33** 1049
[35] Callen J D, Cole A J and Hegna C C 2009 *Phys. Plasmas* **16** 082504
[36] King J D *et al* 2014 *Rev. Sci. Instrum* **85** 083503
[37] da Silva E C, Caldas I L, Viana R L and Sanjuán M A F 2002 *Phys. Plasmas* **9** 4917
[38] Roeder R K W, Rapoport B I and Evans T E 2003 *Phys. Plasmas* **10** 3796
[39] Wingen A, Evans T and Spatschek K 2009 *Nucl. Fusion* **49** 055027
[40] Waelbroeck F 2009 *Nucl. Fusion* **49** 104025